PAPER

Check for updates

Renewable biomass derived porous BCN nanosheets and their adsorption and photocatalytic activities for the decontamination of organic pollutants†

Dan Tu, [a] Huiwei Liao, [*a] Qiulin Deng,[*ab] Xiang Liu,[a] Ronggang Shang[a] and Xiaoyong Zhang[a]

In this work, the preparation, characterization and removal capabilities of a novel biomass derived BC and its BCN nanocomposites are described. Possessing hierarchically porous structures, extremely large surface areas and special chemical bonds, porous BCN nanosheets have demonstrated advantages in terms of their adsorption and photocatalytic activities. The adsorption and photocatalytic activities of the as-prepared catalysts were evaluated by the degradation of RhB. The best results exhibited 97% and 95% decomposition of RhB which were obtained by using porous BCN-40 nanosheets within 120 min at 25 °C under UV light and visible light (>420 nm) irradiation respectively. The rate constant of the porous BCN-40 nanosheets for the degradation of RhB was more 16 times than that of pure h-BN. Besides, the porous BCN nanosheets showed remarkable cycling stability, maintaining a high photocatalytic activity up to 94% after 5 cycles. Furthermore, the degradation mechanisms of RhB and the photocatalytic mechanism have been explained in this paper.

1. Introduction

Much interest has been focused on photocatalytic adsorbing materials because of energy shortages and environmental concerns. In China, the yield of pomelo is huge every year, and a lot of pomelo peel (PP) is disposed of *via* incineration and landfill, which causes serious environmental problems.[1–6] Therefore, there are numerous more environmentally sound methods to reuse these biomasses including PP.[7]

In recent years, biochar (BC) has attracted wide attention because of the abundance of its raw materials, its simple processing and its excellent adsorption performance. Biochar is produced by biomass pyrolysis under hypoxic conditions and it is one type of black carbon.[8–10] Biochar, is a light, black, and fluffy substance composed of C (over 70%), H, O, and N. Biomass-derived BC is widely considered as an adsorptive material for decontamination because of its carboxy groups, phenolic hydroxy groups and many other functional groups.[11] As we all know, water pollution is an unavoidable environmental problem that human beings have to confront, because

the manufacture of daily necessities produces a large amount of toxic wastewater, which poses a big threat to human health and the ecological balance. Therefore, in this research, we show that PP can be used as a precursor of biochar.

In this context, photocatalytic technology cannot be ignored to solve these problems. Traditional photocatalysts are usually metal oxide materials, such as TiO2, ZnO, CdS and MnO2.[12–15] Unfortunately, the band gaps of these metal oxide photocatalysts are generally wide, and can only respond to the shorter wavelengths of visible light or ultraviolet light. Besides, the metal oxide photocatalysts have poor chemical stability and are extremely vulnerable to corrosion, which may cause secondary pollution. Nowadays, the study of non-metal semiconductor photocatalysts has become a hot topic in the field of effective photocatalysis.[16–21] Boron nitride (BN) is called "white graphene" due to its similarities to graphene; it consists of a honeycomb structure of covalently bound boron and nitrogen atoms.[24] It has unique electronic features with a wide band gap of up to 5.5 eV, can be applied as a deep-ultraviolet-light emitter and can be a perfect substitute for graphene based devices.[21–24] It could be a promising support material for catalysts due to its remarkable properties, including an extremely high antioxidant capacity, good chemical inertness, high thermal conductivity, high melting point and high surface area.[25–29] Although BN is not commonly considered as a proper material for photocatalysis and other photo-voltaic conversion applications, it can form boron carbon nitride (BCN). C-doped BN, so-called ternary

School of Materials Science and Engineering, Southwest University of Science and Technology, Mianyang 621010, China. E-mail: liaohw6709@163.com; deng198608@hotmail.com

Jiangsu Provincial Key Laboratory of Palygorskite, Science and Applied Technology, Huaiyin Institute of Technology, Huaian, 223003, China

† Electronic supplementary information (ESI) available. See DOI: 10.1039/c8ra03689f
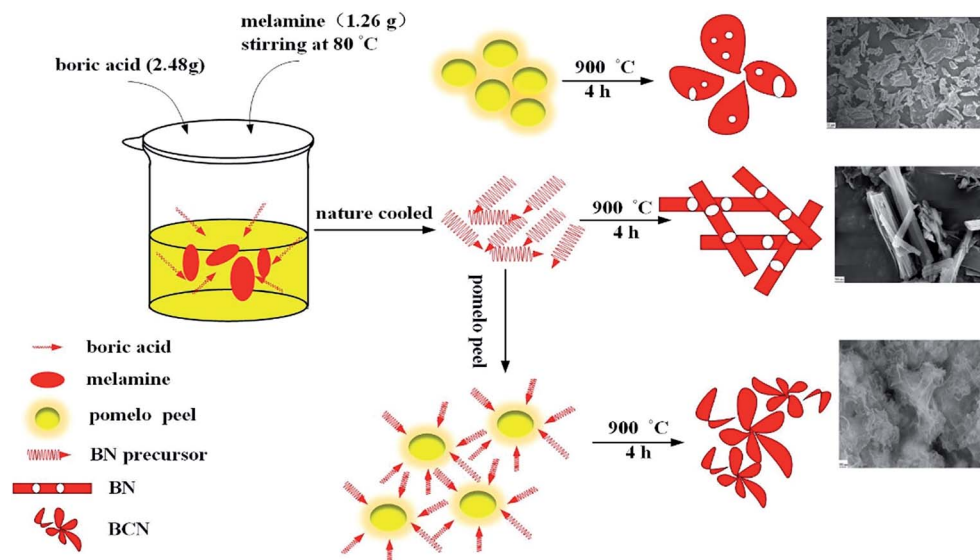
Scheme 1 Schematic illustration for the preparation of BC, BN and BCN.

BCN compounds can form many structures such as nanotubes,[30] nanosheets,[31] nanoporous structures,[32] fibres,[33] *etc.* BCN contains a tunable medium band gap, a large specific surface area, and a surface rich in O-containing groups, unfortunately, research remains in its infancy on its synthesis and photocatalytic performance.[34]

In this research, a facile novel synthesis method will be used to prepare the decontamination material, biomass derived BC modified BN, which produces a ternary structure of porous BCN nanosheets at low temperatures (as shown in Scheme 1). It has both adsorptive and photocatalytic capabilities for the decontamination of organic and inorganic pollutants.

2. Experimental

2.1. Materials

Boric acid (H_3BO_3, Chengdu, China), melamine (Chengdu, China), pomelo peel (collected from a fruit market, Mianyang, China), TiO_2, rhodamine B (RhB), and ethanol. All the reagents were of analytical grade and were used as received without further purification.

2.2. Synthesis of BCN-*x*

Typically, boric acid and melamine with the molar ratio 4 : 1 were dissolved in 40 mL of ultrapure water, after that, the mixed solution was stirred at 80 °C to allow complete reaction, this was then cooled to room temperature to obtain a white flocculent precursor, which was filtered and dried. The precursor (2.0 g) and a certain amount of processed PP powder were fully ground with an agate mortar. Then the mixed precursor was put into an alumina crucible and heated in a tube furnace to 900 °C for 4 h under a N_2 atmosphere. Finally, the as-prepared samples were washed with 0.1 M HCl and dried in an oven. The resulting final catalysts were designated BCN-*x*, where *x* (10, 25, 40, and 60) is the percentage weight content of PP to white flocculent

precursor. When the PP was zero, the synthesized sample was denoted as BN. BC was directly calcined by PP.

2.3. Photodegradation and adsorption experiments

The experiments were carried out using a 350 W GYZ220 xenon lamp (China) with a cut-off filter of 420 nm and an 18 W UV lamp (365 nm, China) as the irradiation source at 25 °C. Catalysts (0.05 g) were added into 200.0 mL of organic dye (0.02 g L^{-1}) solutions in a beaker, respectively. Before irradiation, the mixed solution was put in a completely dark environment for 30 min with magnetic stirring to achieve an adsorption/desorption equilibrium between the dye and photocatalyst. Finally, the photocatalytic system was exposed to UV light and visible-light. During the reaction, vigorous agitation was performed to ensure uniform irradiation of the catalysts. The adsorption experiments were the same as the photodegradation experiments except without irradiation. These took place in a wholly dark environment.

The degradation and adsorption efficiencies of the organic contaminant are measured by using a UV-vis spectrophotometer to detect the absorbance at their maximum absorption wavelength (λ max).[35] The ability of the catalysts would be defined by measuring the degradation efficiency of dye Q, which is defined by the following representation:[35]

$$Q = (C - C_0)/C \times 100\% = (A - A_0)/A \times 100\% \qquad (1)$$

where C is the initial concentration when the adsorption/desorption equilibrium is achieved, C_0 is the concentration at the desired time interval, A and A_0 are corresponding values of absorbancy. Besides, to investigate the radical scavengers, inhibition tests on porous BCN nanosheets were carried out. BQ (0.20 mM) is the scavenger for the superoxide radical, *tert*-butanol (0.20 M) is adopted to quench the hydroxyl radical, and TEOA (0.10 M) is used to explore the hole radical.[36,37]

2.4. Stability testing of the photocatalysts

To evaluate the stability of the porous BCN nanosheets, a recycled usage experiment was designed. The porous BCN-40 nanosheets (0.25 g L^{-1}) were suspended in an aqueous solution of RhB (0.02 g L^{-1}) in a beaker, which was irradiated under an 18 W UV lamp for 120 min. The samples were centrifuged, washed with distilled water and ethanol, dried in an oven at 80 °C and then collected. The reaction was re-initiated using reused BCN-40, a fresh solution of RhB for the second cycle, and then as previously described. This process was repeated up to 5 times.

2.5. Material characterization

The samples were initially measured by Fourier transform infrared (FT-IR) spectroscopy (5700, Japan) and X-ray diffraction using an X-ray diffraction (XRD) analyzer with Cu-Kα radiation (X'Pert PRO, PANalytical). The surface chemical composition of the samples was measured by X-ray photoelectron spectroscopy (XPS), using a Perkin-Elmer model PHI 5600 XPS system. The infrared spectra of the samples were recorded on a Spectrum Spotlight FT-IR Imaging System (PerkinElmer Spectrum One). Ultraviolet visible (UV-vis) diffuse reaction spectra (DRS) were recorded on a UV-vis spectrophotometer (Solidspec-3700, Japan) in the range of 200–800 nm. The more detailed structural information was determined using a field emission scanning electron microscope (FE-SEM, Libra 200), a transmission electron microscope (TEM) and a high-resolution transmission electron microscope (HRTEM, Tecnai F20, FEI). The specific surface area was determined with the BET equation using an adsorption apparatus (NOVA 3000).

3. Results and discussion

3.1. FT-IR and XRD analyses

To confirm the functional groups present in h-BN, BC and porous BCN nanosheets, FT-IR spectra were recorded. In Fig. 1(A), the pattern for pure BN revealed a peak at 806 cm^{-1} which can be assigned to the out-of-plane bending vibration of the B–N–B bond.[38] The peak at 1385 cm^{-1} belongs to the B–N in-plane stretching vibration. This is consistent with the sp^2 replacement of h-BN. The peak at 3437 cm^{-1} and the shoulder around 2972 cm^{-1} can be attributed to the stretching modes of the O–H and N–H groups.[39,40] With biochar, the shoulder peaks at 1071 cm^{-1}, 1251 cm^{-1} and 1624 cm^{-1}, are attributed to the C–OH, C–N and C=N stretching modes, respectively.[41] These functional groups play key roles in the absorption-activation of organic and inorganic molecules. Increasing the amount of biochar narrows the peak of the B–N stretching vibration, along with a slight shifting of the peak for the B–N–B bond to lower angles.

The structures of the samples were investigated using XRD, and the XRD spectra are exhibited in Fig. 1(B). Without biochar, there are three peaks for h-BN at 26.7°, 41.6° and 76.0° in the spectrum, corresponding to the (002), (100) and (110) planes of the h-BN phase (JCPDS no. 34-0421), among which the strongest plane is the (002) plane. The (002) crystal plane proves the existence of a layered structure in h-BN. With biochar, all samples feature XRD peaks that are similar to the main peaks of h-BN, and increasing amounts of biochar broadens the peaks, along with significantly decreasing the intensities of the (002) and (100) diffraction peaks. A slight shift of these peaks to lower angles is seen. This demonstrates the doping of carbon into the h-BN lattice, forming ternary B–C–N alloys.

3.2. Morphology

As shown in Fig. 2, the morphology of the porous BCN-40 nanosheets was investigated using FE-SEM and high resolution TEM (HRTEM). The representative FE-SEM images show that the porous BCN-40 nanosheets have perfectly ultrathin lamellar structures with numerous pores in Fig. 2(A). It can be observed that the morphology of the porous BCN-40 nanosheets is quite different to h-BN or BC. It is composed of ~10 stacked layers with many pores. The average thickness of BCN-40 is 3–4 nm, and this size range is particularly interesting for optoelectronics as the exciton and charge diffusion length.[42] The HRTEM image of the porous BCN-40 nanosheets sample reveals that the interlayer crystal lattice spacing of the porous BCN nanosheets is 0.33 nm, slightly smaller than that of h-BN (0.34
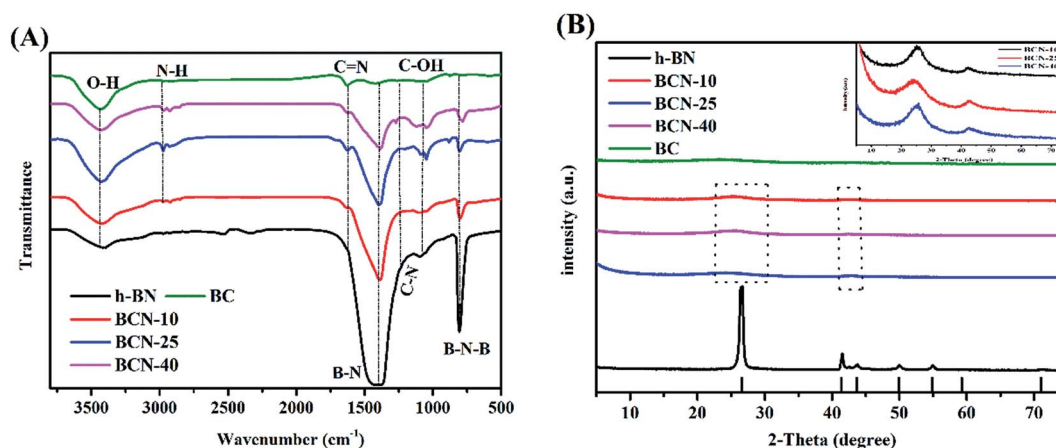

Fig. 1 (A) FT-IR and (B) XRD spectra of h-BN, BC, and porous BCN nanosheets.
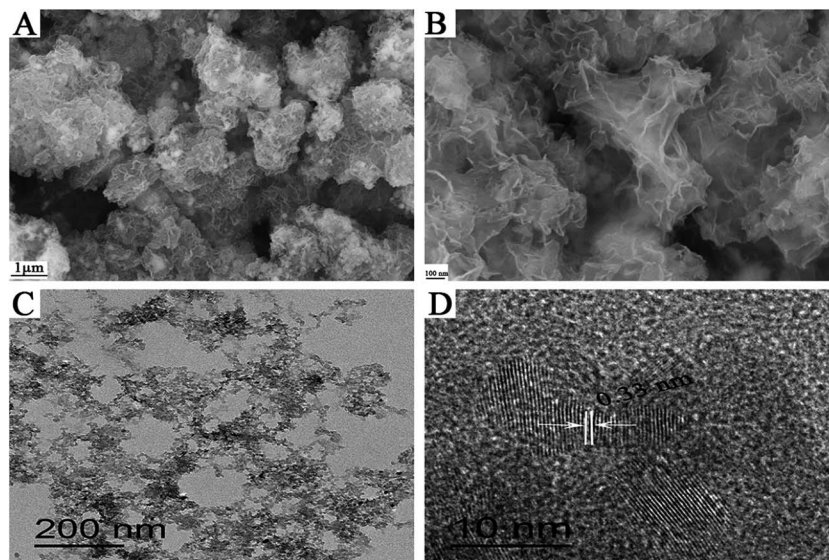
Fig. 2 (A and B) FE-SEM images of BCN-40, (C) TEM image of BCN-40, and (D) HRTEM image of BCN-40.

nm),[43] which is consistent with the XRD results. The results show that the C is doped into the h-BN lattice.[43,44] The element mapping of the porous BCN-40 nanosheets (ESI Fig. 1†) proves the homogeneous distribution of B, C and N elements in the ternary porous BCN-40 nanosheets.

3.3.   XPS analysis

To detect the chemical states of the porous BCN nanosheets, XPS spectra were acquired, which indicate that the four elements of B, C, N, and O exist in porous BCN-40 nanosheets as shown in Fig. 3(A). The main binding energy of B 1s in Fig. 3(B) is centered at 190.9 eV, in which boron is surrounded by nitrogen atoms.[45] The other peaks of B 1s are at 192.6 eV and 189.9 eV, which can be assigned to B–O and B–C bonding, respectively. The spectrum of C 1s in Fig. 3(C) can be deconvoluted into three single peaks, and the main peak at 284.8 eV is ascribed to C=C bonds, which can correspond to the C=C bonds in graphite. The peaks at 286.3 eV and 283.5 eV can be ascribed to C–N and C–B bonds. The N 1s spectrum of the porous BCN-40 nanosheets is illustrated in Fig. 3(D). The dominant peak located at 398.7 eV agrees with the N 1s electron binding energy of the N–C bond. The N–B bonds can also be observed at 397.2 eV. The peak at 399.9 eV corresponds to the N–H bonds, which may also be necessary for edge termination and the reduction of the ammonia atmosphere. So, the above results are fully consistent with the characteristic peaks of BCN.[35] Besides, to better determine the composition and structure of BCN, the XPS spectra of pure BN and BC are also shown in ESI Fig. 3†. The B 1s and N 1s spectra show main binding energies at 190.5 eV, and 398.2 eV, which illustrate a typical crystalline structure related to h-BN and clear BN bonding. The core-level C 1s XPS spectrum of BC shows the presence of various carbon groups such as graphitic carbon (284.6 eV), and carbon nitride (286.5 eV). It can be observed that not only do the porous BCN-40 nanosheets include all electron

binding energies but they also increase the vital binding energies such as for the C–B bond by comparison, which can confirm the formation of BCN by C doped BN once again.

3.4.   UV-vis DRS

To evaluate the optical absorption ability of the as-synthesized porous BCN nanosheets, the DRS spectra give more information regarding the impact of the presence of carbon on h-BN. The BC made as such is a typically strong adsorbent for light of all wavelengths. As shown in Fig. 4(A), although the h-BN made as such is a representative insulator as discussed in the introduction, the absorption wavelengths of the porous BCN nanosheets gradually red-shift as the amounts of BC are increased. The long absorption tails in the DRS spectra are caused by the presence of intraband impurity transitions potentially, especially for BCN-60. The band gap energy is designated by the Kubellka-Munk function, as per the following equation:

$$\alpha h\nu = A(h\nu - E_g)^{1/2} \tag{2}$$

where α is the absorption efficient, h represents Planck's constant, ν is the radiation frequency, and A is a constant.[46] In Fig. 4(B), we obtain a linear plot for $(\alpha h\nu)^{1/2}$ *versus* $h\nu$ whose slope is the band gap value.[46] For the porous BCN nanosheets, the band gaps of the BCN-10, BCN-25 and BCN-40 samples were reduced with increasing amounts of BC, and they showed well-defined absorption edges, revealing their capability to utilize visible and UV light.

3.5.   N₂ adsorption analysis

To investigate the inner structure of the samples, the N_2 adsorption/desorption isotherms were determined (see Fig. 5). The BET surface areas of the samples are shown in ESI Table 1,† which shows many differences. The surface area of h-BN is very
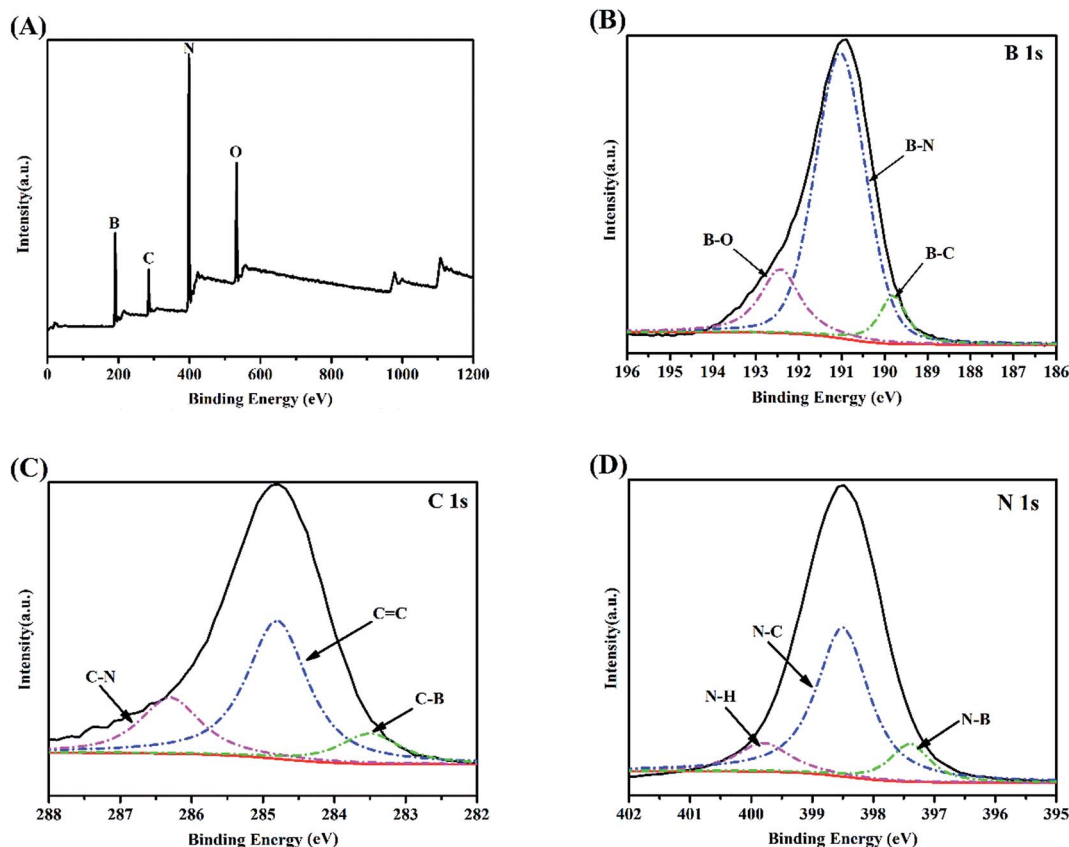
Fig. 3 XPS spectra of the porous BCN-40 nanosheets: (A) survey spectra, (B) B 1s region, (C) C 1s region, and (D) N 1s region.

small, only 2.99 m² g⁻¹, and the surface area of BC is little higher than h-BN. Fortunately, the surface areas of the porous BCN nanosheets obviously increase following the increasing total pore volume. They can cause much higher adsorption and photodegradation performances.

3.6. Adsorption and photocatalytic activity

3.6.1 Adsorption of RhB. The adsorptive behavior of the BC, porous BCN nanosheets and h-BN composites was investigated using a cationic dye (RhB). As shown in Fig. 6(A), the adsorption of RhB by the ternary porous BCN nanosheets was realised. The capability of pure h-BN for the uptake of RhB is very weak. However, the samples clearly exhibit much better adsorption capabilities with the BC incorporated, and the removal percentages of RhB on BCN-10, BCN-25, BCN-40, and BCN-60 are gradually increased. The BCN-60 sample shows the best adsorption rate and capacity (30 wt%), and this sample has the highest percentage of PP (60 wt%). Compared with
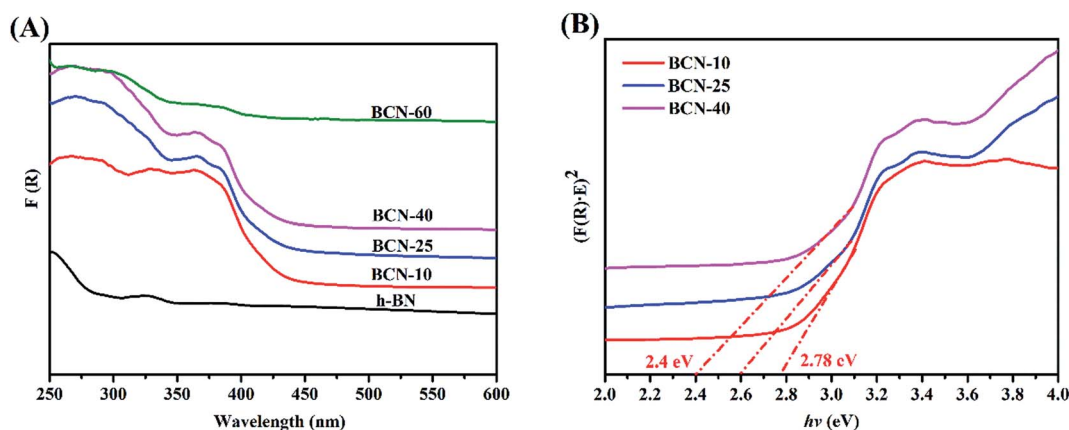

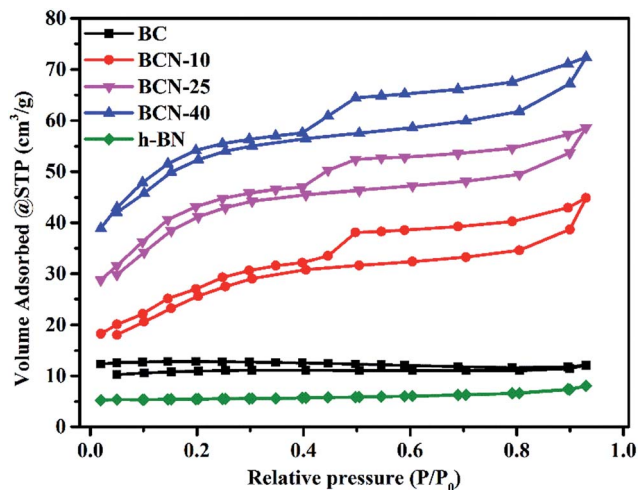Fig. 4 (A) UV-vis (DRS) spectra of the photocatalysts and (B) Tauc plot of the as-prepared photocatalysts.

Fig. 5 N₂ adsorption–desorption isotherms of the BC, porous BCN nanosheets and h-BN samples.

a commercial activated carbon, as shown in Fig. 6(B), the ternary BCN still showed superior adsorption performance. According to the zeta potential measurements in ESI Table 2,† the as-prepared samples basically presented negatively charged surfaces. The negatively charged surfaces of the samples favor the adsorption of cationic dyes *via* electrostatic attraction.[47–50] For the cationic RhB dye, the electrostatic attraction was obviously stimulated and a higher adsorption capacity was anticipated. The introduced functional groups from the BC (as mentioned in Fig. 1), can increase the adsorption capability of the porous BCN nanosheets further.

The adsorption capabilities of the porous BCN nanosheets can be evaluated using the following equation:

$$q_e = \frac{V \times \Delta C_i}{m} \quad (3)$$

where q_e represents the specific adsorption capacity (mg g⁻¹) of the catalyst on the RhB, ΔC_i (mg L⁻¹) is the decline in concentration by adsorption processes, V (L) represents the volume of the reaction solution and m (g) represents the mass of catalyst. It is calculated that the adsorption capacity of the pure h-BN is

only 11.2 mg g⁻¹. Compared with the h-BN, the adsorption capacities of the porous BCN nanosheets are in the range from 14.4 mg g⁻¹ to 24 mg g⁻¹, and the BC in the porous BCN nanosheets represents an inferior capability for RhB adsorption.

3.6.2 Photocatalytic performance of porous BCN nanosheets. Fig. 7 demonstrates the photo-degradation process of RhB in the presence of the porous BCN nanosheets, and provides a distinct comparison between the pure h-BN and porous BCN nanosheets with different amounts of BC. Relative to the adsorption process in the dark, the decolorization is clearly enhanced for the porous BCN nanosheets under UV and visible light irradiation conditions. As shown in Fig. 7(A), the pure h-BN sample achieved only a 19% decolorization after irradiation for 120 min. Notably, the porous BCN nanosheets exhibited much higher decolorization efficiencies compare to pure h-BN, indicating that the BC amount has an important impact on the photocatalytic activity of BCN. When the BC amount was increased to 40 wt%, the porous BCN nanosheets exhibited the best photocatalytic performance, which is a high degradation efficiency of 97% within 120 min under UV light irradiation. Nevertheless, the photocatalytic ability of porous BCN nanosheets slightly decreased when the content of BC increased to 60 wt%. This demonstrates that excess amounts of BC may cover the active sites on the porous BCN nanosheets, thereby causing an unfavourable effect on the generation of charges from BCN. It is desirable to design visible-light-driven photocatalysts. Here, the porous BCN nanosheets (40 wt%) still display high degradation percentages up to 95% for RhB under visible light irradiation (>420 nm), as shown in Fig. 7(B). The porous BCN nanosheets were also applied to the degradation of phenol. As shown in ESI Fig. 2(B),† the degradation percentage of phenol can be up to 89% with porous BCN nanosheets (40 wt%) during the visible light irradiation process. However, only 13% of the phenol was degraded by pure BN under the same conditions. The superior photocatalytic activity of porous BCN nanosheets compared to that of pure BN for both RhB and phenol degradation under visible light irradiation firmly demonstrates their visible-light-driven characteristics, presenting the great potential of these novel hybrid nanosheets.
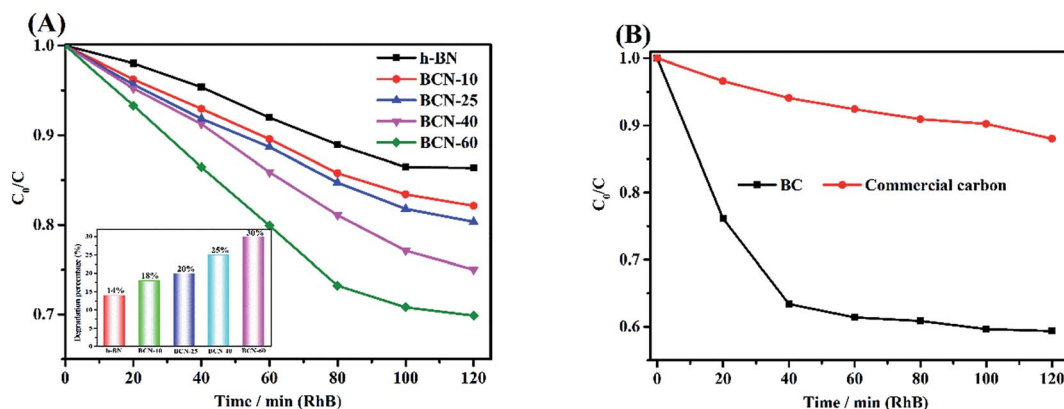

Fig. 6 (A) Adsorption of RhB with h-BN, and porous BCN nanosheets; (B) commercial activated carbon and BC.
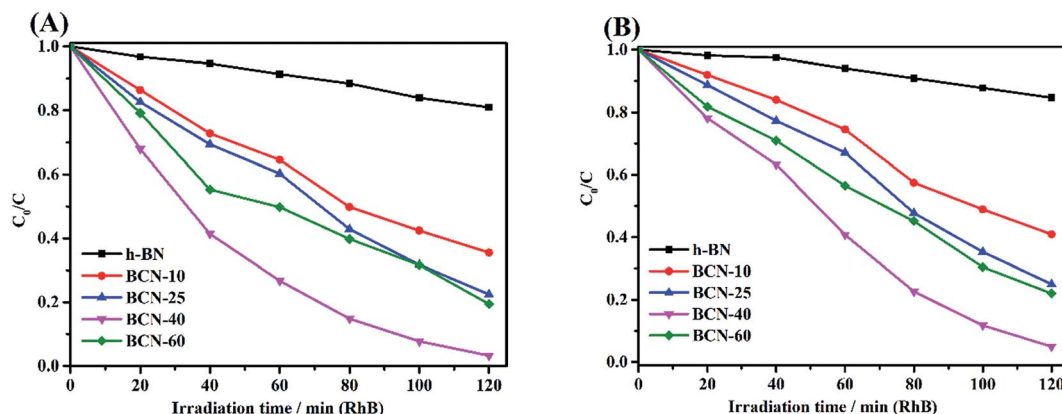
Fig. 7 Photodegradation of RhB by catalysts under different light sources, (A): UV light and (B): visible light.

For comparison, the photocatalytic performance of BCN-40 is compared to other semiconductor photocatalysts. As shown in ESI Fig. 2(A),† blank and comparative experiments were carried out. The results indicate that the self-degradation of RhB could be disregarded under irradiation and that the photocatalytic capability of porous BCN-40 nanosheets is higher than that of g-C_3N_4 and TiO_2. The comparisons of the photocatalytic activities of the porous BCN nanosheets with other semiconductor photocatalysts previously reported for the photocatalytic degradation of RhB are listed in ESI Table 4†. All results show that porous BCN nanosheets have a good effect on the decomposition of pollutants.

The kinetic study was analysed using the kinetic model proposed by Langmuir–Hinshelwood following the equation:[46,51,52]

$$-\ln(c_0/c) = kt \qquad (4)$$

where c is the initial concentration of RhB before irradiation, c_0 is the concentration of RhB after irradiation in the expected time interval, t is the irradiation time, and k is a rate constant. From ESI Fig. 4,† we can observe a linear relationship between $-\ln(c/c_0)$ and t, which indicates that the degradation of RhB fits

first-order kinetics well following irradiation with UV and visible light. And it can be seen that BCN-40 exhibits the highest rate constant (0.02905 min^{-1}), which is almost 16 times higher than that of pure h-BN (0.00176 min^{-1}) in ESI Table 3.† This is attributed to the larger surface area and preferable photocatalytic efficiency among the porous BCN nanosheets.

3.6.3 Stability of the photocatalysts. A quite important practical aspect for porous BCN nanosheets is their recovery ability.[46] To test the stability of BCN-40, recycling experiments were done. As shown in Fig. 8(A), the degradation efficiency of RhB decreases gradually after several cycles because either part of the catalyst is lost during each cycle or some of the active sites on the surface of BCN-40 may be covered by RhB. Fortunately, it is clear that the recycled BCN-40 can still maintain its excellent photocatalytic activity after being reused 5 times. The degradation rates following reuse are 98%, 97%, 96%, 95% and 94% within 120 min, respectively. Moreover, the unirradiated porous BCN nanosheets and the porous BCN nanosheets following the 5th cycle of photocatalytic experiments were characterized by XRD analysis (Fig. 8(B)). It can be seen that the phase of the recycled BCN-40 composite shows almost no obvious discrepancies compared to the fresh one. It is demonstrated that the
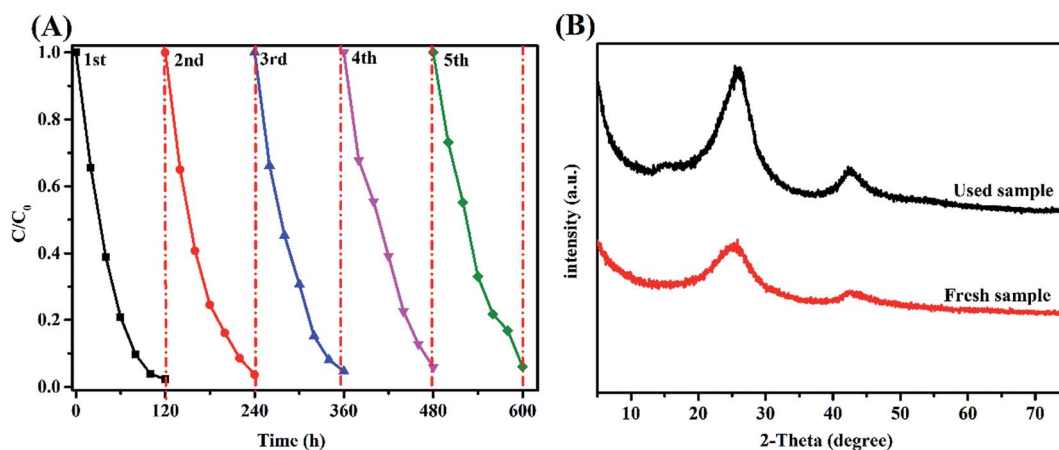

Fig. 8 (A) Photodegradation of RhB by the recycled BCN-40 photocatalyst. (B) The XRD pattern of the fresh BCN-40 sample and used sample.

porous BCN nanosheets are robust and stable photocatalysts. The good recyclability results from the persistence of the photoactivity of the recycled photocatalyst.

3.6.4 Radical trapping experiments. Research using radical scavengers is necessary to understand photocatalytic processes. As can be observed in Fig. 9, the probing through radical trapping control experiments during the reaction over BCN-40 was carried out. It can be shown that the RhB degradation activity of BCN-40 is severely restrained in the presence of TEOA. Besides, BQ has a suppressive effect on the photocatalytic performance and *tert*-butanol only suppresses it to a small extent. The results show that holes play a primary role in the photo-degradation experiments.

3.7. Mechanism of the improved photocatalytic activity of porous BCN nanosheets

Resulting from their high BET surface areas, the porous BCN nanosheets show excellent photocatalytic activities for RhB degradation. The high BET surface areas are of benefit for the prevention of porous BCN nanosheet aggregation, which can endow the photocatalysts with remarkable cyclability.[53] Besides, as shown in Fig. 5 and 6, the higher BET surface areas of porous BCN nanosheets with stronger adsorption abilities can be observed. It is essential to enable the adsorption ability as it is photoinduced reaction species that are dominantly located on their surfaces, which can leave vacancies for RhB adsorption when the adsorbed RhB is gradually degraded during the photocatalytic process. The second factor is the new actively chemical bonding species such as B–N, C–N and C=N after incorporation of BC resulting in conjugate structure changes. As shown in Fig. 3, the porous BCN nanosheets exhibit narrowed band gaps, caused by energy rearrangements during the synthetic processes, so these novel photocatalysts are created with highly efficient light-driven characteristics. In addition, the free radicals on the surfaces are essential for degradation of RhB, as per the following equations:
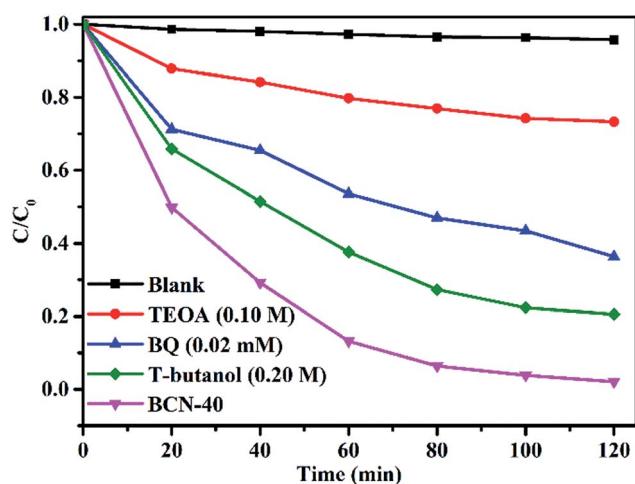

Fig. 9 Inhibition effects of different radical scavengers on the decolorization of RhB: BCN-40 catalysts.
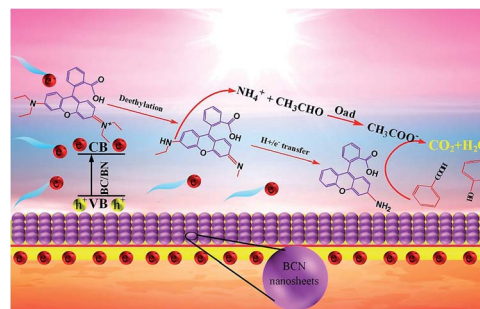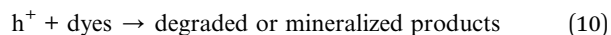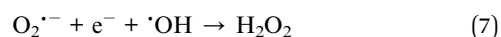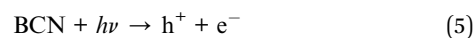

Fig. 10 Structural effects and photodegradation mechanism of RhB over porous BCN nanosheets under irradiation.

$$BCN + h\nu \rightarrow h^+ + e^- \tag{5}$$

$$O_2 + e^- \rightarrow O_2{}^{\cdot-} \tag{6}$$

$$O_2{}^{\cdot-} + e^- + {}^{\cdot}OH \rightarrow H_2O_2 \tag{7}$$

$$H_2O_2 \rightarrow {}^{\cdot}OH \tag{8}$$

$${}^{\cdot}OH(O_2{}^{\cdot-}) + dyes \rightarrow degraded\ or\ mineralized\ products \tag{9}$$

$$h^+ + dyes \rightarrow degraded\ or\ mineralized\ products \tag{10}$$

As shown in Fig. 10, according to the results of the radical trapping experiments and the above analysis, the overall reaction mechanism and process for RhB photocatalytic degradation over the BCN under light irradiation is shown schematically. The RhB photocatalytic degradation proceeds *via* (i) deethylation under the effect of (h^+); (ii) breaking of the RhB central aromatic ring and then the side aromatic rings by the ${}^{\cdot}OH/O_2{}^{\cdot-}$ from the porous BCN nanosheets; (iii) formation of degraded or mineralized products.[54]

4. Conclusion

In summary, we demonstrate that waste biomass can be converted into BC as a carbon source to prepare porous BCN nanosheets at temperatures as low as 900 °C, which not only exhibited high adsorbability (30% adsorbed) but also showed a remarkable photodegradation ability (97% degraded). The BET showed that the BCN nanosheets have a larger specific surface area. UV-vis diffuse reflectance spectra reveal that the absorption edges of the porous BCN nanosheets are adjusted by changing the amount of BC. The porous BCN nanosheets retained their decontamination capability with only a 4% drop in the photodegradation ability observed for porous BCN nanosheets even after 5 cycles of operation. This method for converting waste biomass into BC not only offers new insights for the design of advanced metal-free photocatalysts such as porous BCN nanosheets, but also stimulated us to realize a value-added utilization of waste biomass from nature and the structure-introduced functions endowed by nature, which are of profound significance in achieving efficient environmental protection.

Conflicts of interest

There are no conflicts to declare.

Acknowledgements

References

1 X. Huang, M. Li, J. Li and Y. Song, *Atmos. Environ.*, 2012, **50**, 9–15.

2 S. Yang, H. He, S. Lu, D. Chen and J. Zhu, *Atmos. Environ.*, 2008, **42**, 1961–1969.

3 D. G. Streets, S. Gupta, S. T. Waldhoff, M. Q. Wang, T. C. Bond and B. Yiyun, *Atmos. Environ.*, 2001, **35**, 4281–4296.

4 G. Cao, X. Zhang, S. Gong and F. Zheng, *J. Environ. Sci.*, 2008, **20**, 50–55.

5 K. L. Dionisio, S. R. Howie, F. Dominici, K. M. Fornace, J. D. Spengler, R. A. Adegbola and M. Ezzati, *Environ. Sci. Technol.*, 2012, **46**, 3519.

6 B. Gadde, S. Bonnet, C. Menke and S. Garivait, *Environ. Pollut.*, 2009, **157**, 1554–1558.

7 L. Pi, R. Jiang, W. Zhou, H. Zhu, W. Xiao, D. Wang and X. Mao, *Appl. Surf. Sci.*, 2015, **358**, 231–239.

8 A. R. Mohamed, M. Mohammadi and G. N. Darzi, *Renewable Sustainable Energy Rev.*, 2010, **14**, 1591–1599.

9 X. Tan, Y. Liu, G. Zeng, X. Wang, X. Hu, Y. Gu and Z. Yang, *Chemosphere*, 2015, **125**, 70–85.

10 M. Kılıç, Ç. Kırbıyık, Ö. Çepelioğullar and A. E. Pütün, *Appl. Surf. Sci.*, 2013, **283**, 856–862.

11 H. Zhou, B. Yan, J. Lai, H. Liu, A. Ma, W. Chen, X. Jin, W. Zhao and G. Zhang, *J. Ind. Eng. Chem.*, 2018, **58**, 334–342.

12 S. Li, X. Shen, J. Liu and L. Zhang, *New J. Chem.*, 2017, **42**, 1155.

13 Z. Yue, A. Liu, C. Zhang, J. Huang, M. Zhu, Y. Du and P. Yang, *Appl. Catal., B*, 2017, **201**, 202–210.

14 S. Li, S. Hu, W. Jiang, Y. Liu, Y. Zhou, Y. Liu and L. Mo, *J. Colloid Interface Sci.*, 2018, **521**, 42–49.

15 S. Li, S. Hu, K. Xu, J. Wei, J. Liu and Z. Wang, *Nanomaterials*, 2017, **7**(1), 22.

16 R. K. Nath, M. F. M. Zain and M. Jamil, *Renewable Sustainable Energy Rev.*, 2016, **62**, 1184–1194.

17 L. Liu, Y. Zhou, X. Zhao, H. Wang, L. Wang, G. Yuan, M. Asim, W. Wang, L. Zeng and X. Liu, *Dev. Comp. Immunol.*, 2014, **47**, 17–24.

18 S. N. Kulikov, V. E. Tikhonov, E. A. Bezrodnykh, S. A. Lopatin and V. P. Varlamov, *Russ. J. Bioorg. Chem.*, 2015, **41**, 57–62.

19 K. M. Lee, C. W. Lai, K. S. Ngai and J. C. Juan, *Water Res.*, 2016, **88**, 428–448.

20 W. Lei, D. Liu and Y. Chen, *Adv. Mater. Interfaces*, 2015, **2**(12), 1500228.

21 C. A. Lin, J. C. S. Wu, J. W. Pan and C. T. Yeh, *J. Catal.*, 2002, **210**, 39–45.

22 G. Postole, M. Caldararu, N. I. Ionescu, B. Bonnetot, A. Auroux and C. Guimon, *Thermochim. Acta*, 2005, **434**, 150–157.

23 Q. Weng, Y. Ide, X. Wang, X. Wang, C. Zhang, X. Jiang, Y. Xue, P. Dai, K. Komaguchi and Y. Bando, *Nano Energy*, 2015, **16**, 19–27.

24 R. Najafabadi and D. J. Srolovitz, *Surf. Sci.*, 1994, **317**, 221–234.

25 Y. Xie, Y. Dai, X. Yuan, L. Jiang, L. Zhou, Z. Wu, J. Zhang, H. Wang and T. Xiong, *J. Colloid Interface Sci.*, 2018, DOI: 10.1016/j.jcis.2018.04.031.

26 W. Xie, M. Zhang, D. Liu, W. Lei, L. Sun and X. Wang, *J. Photochem. Photobiol., A*, 2017, **333**, 165–173.

27 D. Liu, L. He, W. Lei, K. D. Klika, L. Kong and Y. Chen, *Adv. Mater. Interfaces*, 2015, **2**, 1500228.

28 Y. Tao, N. Qian, M. Wei, D. Xia, X. Li and A. Xu, *RSC Adv.*, 2015, **5**, 185–186.

29 C. Zhi, Y. Bando, C. Tang, H. Kuwahara and D. Golberg, *Adv. Mater.*, 2010, **21**, 2889–2893.

30 W. Lei, V. N. Mochalin, L. Dan, Q. Si, Y. Gogotsi and C. Ying, *Nat. Commun.*, 2015, **6**, 8849.

31 T. M. Schmidt, R. J. Baierle, P. Piquini and A. Fazzio, *Phys. Rev. B*, 2003, **67**, 181–183.

32 C. Zhao, Z. Xu, H. Wang, J. Wei, W. Wang, X. Bai and E. Wang, *Adv. Funct. Mater.*, 2015, **24**, 5985–5992.

33 W. Lei, D. Portehault, D. Liu, S. Qin and Y. Chen, *Nat. Commun.*, 2012, **4**, 1777.

34 M. Yano, M. Okamoto, Y. K. Yap, M. Yoshimura, Y. Mori and T. Sasaki, *Diamond Relat. Mater.*, 2000, **9**, 512–515.

35 C. Huang, C. Chen, M. Zhang, L. Lin, X. Ye, S. Lin, M. Antonietti and X. Wang, *Nat. Commun.*, 2015, **6**, 7698.

36 Y. Wang, J. Yao, H. Li, D. Su and M. Antonietti, *Cheminform*, 2011, **42**(27), DOI: 10.1002/chin.201127041.

37 L. Zhou, W. Song, Z. Chen and G. Yin, *Chemical Hazards in Industry*, 2013, **47**, 3833–3839.

38 J. Di, J. Xia, M. Ji, B. Wang, S. Yin, Y. Huang, Z. Chen and H. Li, *Appl. Catal., B*, 2016, **188**, 376–387.

39 S. Ikeda, N. Sugiyama, S. Y. Murakami, H. Kominami, Y. Kera, H. Noguchi, K. Uosaki, T. Torimoto and B. Ohtani, *Phys. Chem. Chem. Phys.*, 2003, **5**, 778–783.

40 C. S. LianchengWang, L. Xu and Y. Qian, *Catal. Sci. Technol.*, 2011, **1**, 1119–1123.

41 A. S. Rozenberg, Y. A. Sinenko and N. V. Chukanov, *J. Mater. Sci.*, 1993, **28**, 5675–5678.

42 M. Kovacevic, S. Agarwal, B. L. Mojet, J. G. V. Ommen and L. Lefferts, *Appl. Catal., A*, 2015, **505**, 354–364.

43 S. R. Forrest, *MRS Bull.*, 2005, **30**, 28–32.

44 W. Lei, D. Portehault, R. Dimova and M. Antonietti, *J. Am. Chem. Soc.*, 2011, **133**, 7121–7127.

45 P. Niu, L. Zhang, G. Liu and H. M. Cheng, *Adv. Funct. Mater.*, 2012, **22**, 4763–4770.

46 H. C. Choi, S. Y. Kim, W. S. Jang, S. Y. Bae, J. Park, K. L. Kim and K. Kim, *Chem. Phys. Lett.*, 2004, **399**, 255–259.

47 Y. Jiang, Z. Jin, C. Chen, W. Duan, B. Liu, X. Chen, F. Yang and J. Guo, *RSC Adv.*, 2017, **7**, 12856–12870.

48 L. Gao, H. Yin, H. Zhu, X. Mao, F. Gan and D. Wang, *Sep. Purif. Technol.*, 2014, **129**, 113–120.

49 Y. Yao, B. Gao, M. Inyang, A. R. Zimmerman, X. Cao, P. Pullammanappallil and L. Yang, *Bioresour. Technol.*, 2011, **102**, 6273–6278.

50 A. Mukherjee, A. R. Zimmerman and W. Harris, *Geoderma*, 2011, **163**, 247–255.

51 M. Shanmugam, R. Jacobs-Gedrim, C. Durcan and B. Yu, *Nanoscale*, 2013, **5**, 11275–11282.

52 Y. Yang, L. Geng, Y. Guo, J. Meng and Y. Guo, *Appl. Surf. Sci.*, 2017, **425**, 535–546.

53 Y. Ide, F. Liu, J. Zhang, N. Kawamoto, K. Komaguchi, Y. Bando and D. Golberg, *J. Mater. Chem. A*, 2014, **2**, 4150–4156.

54 D. Liu, M. Zhang, W. Xie, L. Sun, Y. Chen and W. Lei, *Appl. Catal., B*, 2017, **207**, 72–78.